Low temperature catalytic reverse water-gas shift reaction over perovskite catalysts in DBD plasma

Lina Liu [a], Sonali Das [a], Tianjia Chen [a], Nikita Dewangan [a], Jangam Ashok [a], Shibo Xi[b, c], Armando Borgna[b, c], Li Ziwei [a], Sibudjing Kawi [a, *]

[a] *Department of Chemical & Biomolecular Engineering, National University of Singapore, Singapore 117585*

[b] *Singapore Synchrotron Light Source, National University of Singapore, Singapore 117603*

[c] *Institute of Chemical and Engineering Sciences, A*STAR, 1 Pesek Road, Jurong Island, Singapore 627833*

[*] Corresponding author.

E-mail address: chekawis@nus.edu.sg (Kawi Sibudjing)

Graphic Abstract

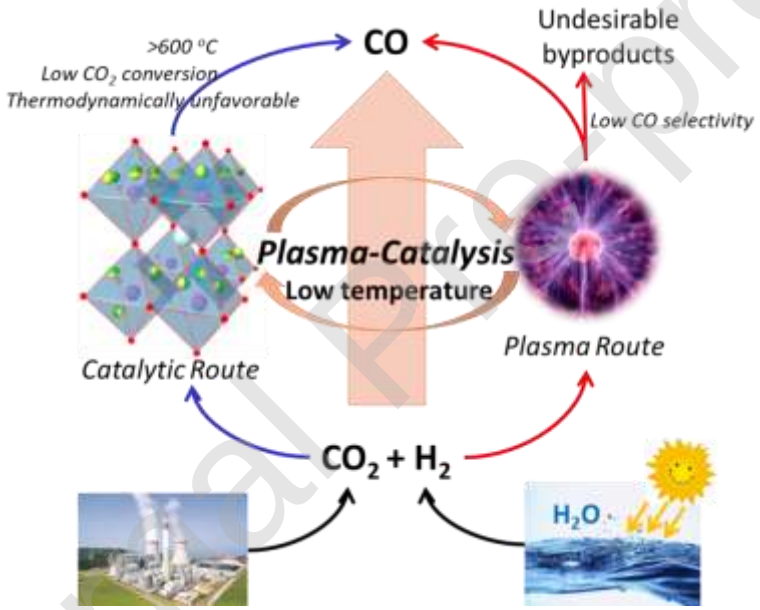

Highlihts

- The hybrid DBD plasma-catalysis system is promising for RWGS at low temperature.
- LSNFO shows the highest potential in promoting the selective conversion of CO_2 to CO.
- The Ni-Fe alloy and oxygen vacancies in LSNFO contribute to its superior performance.
- A H_2/CO_2 ratio of 2:1 is the most promising with the highest CO yield of 56%.

[*] Corresponding author.

E-mail address: chekawis@nus.edu.sg (Kawi Sibudjing)

Abstract

With the aim of eliminating the serious environmental concern arising from excessive anthropogenic CO_2 emission, a hybrid dielectric barrier discharge plasma-catalysis system was developed for the thermodynamic unfavorable reverse water-gas shift reaction at low temperature of < 150 °C. A series of perovskite catalysts including $LaNiO_3$, $La_{0.9}Sr_{0.1}NiO_{3+\delta}$, $La_{0.9}Sr_{0.1}FeO_{3+\delta}$ and $La_{0.9}Sr_{0.1}Ni_{0.5}Fe_{0.5}O_{3+\delta}$ were synthesized, as well as the impregnated Ni/La_2O_3 as a reference. Among, $La_{0.9}Sr_{0.1}Ni_{0.5}Fe_{0.5}O_{3+\delta}$ exhibited the highest potential in promoting the selective conversion of CO_2 to CO, and simultaneously suppressing the formation of CH_4. Its superior catalytic performance should be attributed to that (1) higher metal dispersion, smaller particle size, stronger metal-support interaction and electronically richer state of Ni were achieved by the formation of Ni-Fe alloy, which facilitated the adsorption and conversion of CO_2, and (2) more oxygen vacancies and higher oxygen mobility were created by the remaining $La_{0.9}Sr_{0.1}FeO_{3+\delta}$ perovskite structure, which promoted the selective conversion of CO_2 to CO.

Key words: Perovskite; DBD plasma; RWGS; oxygen vacancy; Ni-Fe alloy

1. Introduction

Ocean acidification and climate changes arising from the excessive emission of anthropogenic carbon dioxide (CO_2) are considered as two of the most serious global environmental concerns [1, 2]. Therefore, the development of CO_2 reduction and reuse technologies is becoming an urgent and important issue to mitigate the risk [3]. In recent years, the utilization of CO_2 as a cheap, nontoxic and abundant C1 building block has attracted growing attention for the synthesis of valuable chemicals and fuels [4]. Among different options, CO_2 hydrogenation has been intensively studied, since numerous valuable products can be achieved including C1 molecules (CH_4 and CH_3OH) to heavier hydrocarbons and alcohols [5]. During CO_2 hydrogenation, the reverse water-gas shift reaction (RWGS) (Eq. 1) is one of the most promising processes for the conversion of CO_2 to obtain CO [6], which together with H_2 as syngas, can be used for the synthesis of methanol, dimethylether (DME), ethanol and Fischer-Tropsch fuels [7, 8].

$$CO_2 + H_2 \rightarrow CO + H_2O \qquad \Delta H^0 = 41.27 \text{ kJ/mol} \qquad (1)$$

RWGS is an moderately endothermic process, which should be operated at high temperatures, and the equilibrium conversion of CO_2 is limited to ~23% at 300 ^oC and 1 MPa [9]. In order to achieve a CO_2 conversion of 50%, a temperature of over 700 ^oC is required with a stoichiometric composition of the feed gas [10]. In addition, RWGS reaction is always accompanied by a competitive methanation process, which decreases the efficiency of the following syngas utilization [11]. Currently, catalytic conversion has been the most widely used strategy for RWGS reaction. Various types of catalysts have been employed including Ni, Cu, Pt, Au, Ru, Rh, Ir and bimetallic catalysts [12-14]. Noble metal catalysts are proven to be highly reactive for this reaction. Porosoff et al. [15] found that the $PtCo/CeO_2$ catalysts showed higher potential in promoting the selective formation of CO compared with other monometallic and bimetallic, due to its lower surface d-band center. However, the high cost of noble metals becomes the major constraint for their large scale application. Non-noble metal catalysts are also developed for RWGS reaction, including Cu, Ni, Fe and Co-based catalysts [1, 3]. The main problems of these catalysts are their lower activity and rapid deactivation caused by fierce aggregation at high temperatures [16]. Therefore, further efforts are still required to develop efficient catalysts with higher activity and stability and potential processes to overcome the slow kinetics and reduce the reaction temperature.

Non-thermal plasma (NTP) is a promising and attractive alternative to conventional catalysis system for RWGS due to its fast ignition, compact design, low operation temperature and high reactivity. Highly reactive species and energetic electrons produced by plasma promote the activation of molecular species and the cleavage of chemical bonds, which enable the occurrence of thermodynamically unfavorable reactions even at ambient conditions [17]. NTP has been extensively applied in a variety of aspects including the removal of atmospheric pollutants, reforming of hydrocarbons and CO_2 conversion [18-20]. However, the main drawbacks of NTP are the formation of rich byproducts and poor selectivity of desired products. Therefore, the combination of NTP and heterogeneous catalysis was considered to be of great potential to overcome both disadvantages of separate thermal catalysis and NTP processes. However, to the best of our knowledge, there are few papers about using NTP in catalytic RWGS and the knowledge of choosing efficient catalysts for plasma-catalytic RWGS is still very limited.

Recently, various attempts have been focused on developing novel and efficient catalysts for thermal catalytic RWGS. Bobadilla et al. [21] demonstrated that the superior performance of Au/TiO_2 for RWGS should be attributed to its higher concentration of oxygen vacancies, which promoted the effective activation of CO_2 and proceeding of RWGS via redox mechanism. It was reported by Kim et al. [22] that the activity of Pt/TiO_2 for RWGS was primarily dependent on the redox properties of the support, rather than the structure or dispersion of Pt sites. It can be concluded that the oxygen vacancies and redox property of catalysts play a crucial role in the binding and conversion of CO_2 during RWGS reaction. Therefore, perovskite-type catalysts with general chemical formula of ABO_3 are considered to be significantly promising since they are well-known for its abundant oxygen vacancies with the partial substitution of A site and B site metals, resulting in the lattice distortion and oxygen nonstoichiometry [23]. Kim et al. [24] studied RWGS over parent barium zirconate-based perovskite catalysts doped with Y, Zn, and Ce. The result indicated that $BaZr_{0.8}Y_{0.16}Zn_{0.04}O_3$ catalyst showed the most superior performance with an average CO_2 conversion of 37.5% and a CO selectivity of 97% at 600 ^oC. A series of $La_{1-x}Sr_xCoO_{3-\delta}$ was synthesized by Daza et al. [25] and applied for chemical looping RWGS. Among $La_{0.75}Sr_{0.25}CoO_{3-\delta}$ showed the most superior structure stability under reducing atmospheres and the highest CO production capacity during reoxidation by CO_2. However, the performance of perovskites in plasma-catalytic RWGS was rarely reported.

In this study, Ni-based $LaNiO_3$ perovskite was selected due to the relative higher activity and economic flexibility of Ni [4]. In addition, the additional effect of Sr on A site and Fe on B site was investigated, since it was previously reported that the partially replacement of A site by Sr enabled more oxygen vacancies and more basic sites [23]. Fe was proven to promote the catalytic activity of Ni significantly due to the formation of Ni-Fe alloy and electronic effect created via metal-metal interactions, which facilitated the CO_2 adsorption [4]. Dielectric barrier discharge (DBD) plasma was selected since it is much easier to be integrated with catalysts [26, 27]. Various characterizations of fresh and reduced catalysts were performed, in order to elucidate the mechanism of RWGS in the hybrid DBD-perovskite catalysis system.

2. Materials and methods

2.1 Synthesis of catalysts

A series of perovskite catalysts were prepared by sol-gel method, using citric acid as the complexing agent. Stoichiometric amounts of $La(NO_3)_2 \cdot 6H_2O$ (Sigma–Aldrich), $Sr(NO_3)_2 \cdot 6H_2O$ (Sigma–Aldrich), $Ni(NO_3)_2 \cdot 6H_2O$ (Merck) and $Fe(NO_3)_3 \cdot 9H_2O$ (Aldrich), citric acid monohydrate (Sigma–Aldrich) and ethylene glycol were weighed and dissolved in deionized water. The molar ratio of mixed lanthanum–strontium to citric acid monohydrate was 1:2, while the molar ratio of citric acid monohydrate to ethylene glycol was 1:1. The obtained solution was stirred continuously at 80 ^oC until a viscous gel was formed. Then the samples were dried at 100 ^oC overnight, followed by calcined at 800 ^oC for 6 h. Three perovskite catalysts of $LaNiO_3$, $La_{0.9}Sr_{0.1}NiO_{3-\delta}$, $La_{0.9}Sr_{0.1}FeO_{3-\delta}$ and $La_{0.9}Sr_{0.1}Ni_{0.5}Fe_{0.5}O_{3-\delta}$ were prepared by this method, which are referred to as LNO, LSNO, LSFO and LSNFO in the following content. In addition, Ni/La_2O_3 catalyst with a Ni loading of around 26.5% (same with reduced LNO) was prepared by wetness impregnation and used as a reference to compare the performance of perovskite catalysts for RWGS.

2.2 Experimental setup

Fig. S1 shows the experimental setup of RWGS in a hybrid DBD plasma-catalysis system, which is operated at atmospheric pressure and low temperature. A threaded stainless steel rod (O.D.=16 mm) served as the high-voltage electrode of the DBD plasma, and a wire mesh with a length of 150 mm, which is wrapped over a quartz tube (inner diameter: 20 mm, thickness: 2.5 mm) acted as the ground electrode. A CTP-2000K power supply (Coronalab, Nanjing, China) with a maximum peak to peak voltage of 30 kV and a frequency of 10kHz was connected to the DBD plasma reactor. 100 mg of catalysts diluted by 400 mg inert SiO_2 held by quartz wool was installed in the discharge gap of the DBD plasma reactor. Prior to use, the catalysts were pre-reduced in H_2 (20 ml/min) at 700 ^oC for 1 h. A mixture H_2 and CO_2 with different H_2/CO_2 molar ratios (4:1, 2:1, 1:1, 1:2 and 1:4) was passed through the reactor with a total flowrate of 20 ml/min, and He (10 ml/min) served as the carrier gas. The RWGS reaction was conducted at different discharge powers. The temperatures of DBD plasma reactor at different discharge powers were in the range of 35-120 ^oC (**Fig. S2**), which were monitored by a thermocouple based on previous studies [28, 29]. The

temperature was measured at the outside tube of the reactor, since a thermocouple inside the catalyst bed interferes with the discharge. The gas temperature at the outlet was also monitored [30, 31], which was around 5-15 ^{o}C lower than that of the reactor.

The products of RWGS were condensed in an ice-water trap and then analyzed by an on-line gas chromatograph (6890A, Agilent Technologies, USA.). Besides, the gas products of RWGS over LNO and LSNFO were analyzed on line by a Fourier transform infrared (FTIR) spectrograph, in order to demonstrate the reaction mechanism. The detailed procedure for FTIR analysis has been presented in the supplementary information. The stability test of LSNFO was also conducted with a H_2/CO_2 molar ratio of 2:1 at 89 W. In addition, the RWGS in thermal catalysis system was also investigated as a reference in the temperature range of 400-600 ^{o}C with 100 mg LSNFO diluted by 400 mg SiO_2.

2.3 Characterization of catalysts

The fresh calcined and reduced Ni/La_2O_3, LNO, LSNO and LSNFO catalysts were characterized by different methods as follows. The characterizations of LSFO were not conducted in detail since the conversion of CO_2 over LSFO was even lower than that in plasma reactor without any additives.

The XRD patterns of fresh calcined and reduced catalysts were performed by a Shimadzu XRD-6000 diffractometer using a Cu Kα radiation. The samples were scanned in a 2θ range of 10-80 ^{o} with a speed of 2 ^{o}/min.

H_2 Temperature-programmed reduction (H_2-TPR) was analyzed by a Thermo Scientific TPDRO 1100 series system equipped with a thermal conductivity detector (TCD). For each test, 50 mg of fresh calcined catalysts was heated to 950 ^{o}C with a heating rate of 10 ^{o}C/min in 5% H_2 diluted in N_2 (30 ml/min) after degassing in helium for 10 min.

H_2-chemisorption analysis was conducted to determine the dispersion of different catalysts. Specifically, 50 mg of each fresh catalyst were reduced at 700 ^{o}C in 5% H_2 diluted in N_2 for 1h, and then pulses of H_2 were injected with a known volume until no further uptakes of H_2. The dispersion of active metals was calculated by the ratio of moles of surface Ni atoms to moles of total Ni atoms.

The moles of surface Ni atoms were determined by the amount of H_2 chemisorbed on the catalysts assuming that one hydrogen atom is adsorbed on one surface Ni atom.

Morphology and structure of reduced catalysts was characterized using a JEOL JEM-2100 transmission electron microscopy (TEM) and field emission scanning electron microscopy (FESEM). The samples were ultrasonically dispersed in ethanol and spread over perforated copper grids prior to the TEM analysis.

The specific surface area of calcined and reduced catalysts was measured at 77 K by a N_2 adsorption/desorption instrument (Quantachrome Autosorb-6B) and calculated by Brunauer–Emmett–Teller (BET) method. The pore size and volume was calculated using the Barrett–Joyner–Halenda (BJH) method. Prior to the analysis, the catalysts were degassed in vacuum at 200 ^oC for 6 h to remove the moisture and adsorbed gases.

CO_2-temperature programmed desorption (CO_2-TPD) was carried out in a Thermo Scientific TPDRO 1100 series. 200 mg of catalyst was reduced under the same condition as for the activity test. After cooling down to 50 ^oC in He, purified CO_2 was injected until the adsorption equilibrium. Then the catalyst was heated up to 950 ^oC with a ramping rate of 10 ^oC/min in He flow and the desorbed CO_2 was measured by a TCD detector.

For O_2-TPD, 200 mg of catalyst was reduced at 700 ^oC for 1h, and subsequently pure oxygen was introduced when the temperature reached 300 ^oC for 1h. Then He was injected to purge the remaining oxygen and cool the system to room temperature. The O_2-TPD was performed from 50 to 950 ^oC with He as carrier gas.

X-ray photoelectron spectroscopy (XPS) of reduced catalysts was performed using a Kratos AXIS Ultra DLD, employing a monochromatic Al Kα source (hυ=1486.6 eV) source at 225 W. The C1s (284.6 eV) photoelectron peak was used for the charge calibration.

X-ray absorption spectroscopy (XAS) of reduced LSNFO and LNO were carried out at XAFCA beamline of Singapore Synchrotron Light Source under transmission mode. Ni and Fe standard foil was used for the energy calibration.

Attenuated total reflectance (ATR) analysis was performed in a Bruker FTIR unit. All the samples were treated in the DBD plasma reactor and then were analyzed at room temperature. The amount of sample used for the analysis was around 10 mg.

All catalysts were reduced at 700 ^{o}C for 1h in the atmosphere of hydrogen (20 ml/min) prior to the analysis of reduced catalysts.

2.4 Definitions and calculations

For the RWGS reaction, the conversion of CO_2 was calculated as follows:

$$X(CO_2)(\%)=\frac{\text{moles of } CO_2 \text{ input-moles of } CO_2 \text{ output}}{\text{moles of } CO_2 \text{ input}}\times 100\% \quad (1)$$

The selectivity of CO and CH_4 was defined as Eq. (2) and (3).

$$S(CO)(\%)=\frac{\text{moles of CO output}}{\text{moles of } CO_2 \text{ converted}}\times 100\% \quad (2)$$

$$S(CH_4)(\%)=\frac{\text{moles of } CH_4 \text{ output}}{\text{moles of } CO_2 \text{converted}}\times 100\% \quad (3)$$

The yield of CO was calculated as Eq (4).

$$Y(CO)(\%)=X(CO_2)\times S(CO)\times 100\% \quad (4)$$

3. Results and discussions

3.1 Catalyst characterization

3.1.1 XRD analysis

Fig. 1 shows the wide-angle XRD patterns of fresh calcined and reduced Ni/La_2O_3, LNO, LSNO, LSFO and LSNFO catalysts. As shown in **Fig. 1a**, LNO presented a diffraction pattern of pure perovskite phase (PDF-34-1181) with the main peak at around 2θ=33^{o} [32]. The addition of Sr resulted in the presence of a small diffraction peak of NiO at 2θ=43.2^{o} (PDF-44-1159) in the XRD pattern of fresh LSNO, since the doping of Sr might hindered the interaction of Ni-La_2O_3, and resulted in the formation of NiO [23]. The LSFO and LSNFO both maintained a pure perovskite structure with the substitution of Sr in the A site and Fe in the B site. No obvious diffraction peaks of strontium oxide and iron oxide were detected, suggesting that Sr and Fe were completely incorporated in the perovskite structure. However, the main peak of LSNFO was slightly shifted to lower angle of 32^{o}, indicating the augmentation of lattice spacing and expansion of the perovskite lattice because of the substitution of partial Ni by Fe with larger atomic radius [33]. For the

impregnated Ni/La_2O_3 catalyst, the diffraction peaks of perovskite could also be observed at 2θ=32.8º, 47.3º and 58.7º. However, the simultaneous appearance of NiO at 2θ=43.2º (PDF-44-1159) and La_2O_3 at 2θ=26.1º, 29.3º, 30º, 39.5º, 46º, 52.1º and 55.5º (PDF-05-0602) indicated that the Ni/La_2O_3 was an inhomogeneous mixture.

Fig. 1b shows that the reduced Ni/La_2O_3, LNO and LSNO catalysts show absolutely different XRD patterns from that of the fresh catalysts, indicating that the perovskite structure has been completely collapsed to form metallic Ni supported on La_2O_3. However, the XRD pattern of reduced LSFO still showed a pure perovskite phase, suggesting the structure stability of LSFO. In addition, partial perovskite structure (PDF-37-1493) was still maintained for LSNFO after reduction, corresponding to the presence of LSFO [23], which will be further confirmed by the CO_2-TPD results. The result is different from previous literature reported by Oemar et al. [23]. They found that the perovskite structure of $La_{0.8}Sr_{0.2}Ni_{0.8}Fe_{0.2}O_3$ was completely destroyed after reduction at 600 ºC in purified H_2 flow (30 ml/min). The result suggests that the LSNFO perovskite with a Ni/Fe ratio of 1:1 exhibited a much more stable structure, which could prevent the complete collapse of perovskite structure even at high reduction temperature of 700 ºC. In addition, the peak of La_2O_3 can also be observed for LSNFO. However, the peak intensity of La_2O_3 was obviously reduced, which should be explained by that the presence of LSFO perovskites helps to prevent the phase transformation from amorphous to crystalline La_2O_3 [34]. Kathiraser et al. [34] has confirmed that the presence of octahedral Al^{3+} ions in the $LaAlO_3$ matrix prevent the transformation from γ- to α-Al_2O_3, impact extra stability of Ni/$LaAlO_3$-Al_2O_3 compared with Ni/Al_2O_3 for dry reforming of methane.

The diffraction peak of metallic Ni at 2θ=44.6º (PDF-04-0850) was shifted slightly to lower angles of 43.95º for LSNFO (as presented in **Fig. 1(c)**), which could be explained by the creation of defect sites in the metallic Ni phase by Fe species, consequently leading to the formation of a Ni-rich Ni−Fe alloy with a face-centered-cubic (fcc) structure (PDF-38-0419) [35]. In addition, the intensity of the metallic phase (Ni and Ni-rich Ni-Fe alloy) at 2θ=43.5-45.5º decreased following the order of Ni/La_2O_3 > LNO > LSNO > LSNFO, which should be attributed to the decrease of the crystal size [36]. Their corresponding crystal size of metallic particles was 26.6 nm, 19.7 nm, 16.9 nm and 13.9 nm, respectively, determined by the Debye-Scherrer equation (**Table 1**).

3.1.2 H_2-TPR and H_2-chemisorption analysis

The redox properties and the metal-support interactions of catalysts was investigated using H_2-TPR analysis, as shown in **Fig. 1(d),** as well as the effect of promoters on the reducibility of Ni species in the multi-component catalysts. Two main processes proceeded during the reduction of LNO perovskite as follows:

$$LaNiO_3 + 1/2\ H_2 \rightarrow LaNiO_{2.5} + 1/2\ H_2O \quad (5)$$

$$LaNiO_{2.5} + 1/2\ H_2 \rightarrow La_2O_3 + Ni + 1/2\ H_2O \quad (6)$$

The first peak at around 395 ^oC in the profile of LNO should be attributed to the reduction of Ni^{3+} stabilized in the perovskite structure to Ni^{2+} with the formation of oxygen deficient $LaNiO_{2.5}$. The second peak at around 560 ^oC should be assigned to the reduction of Ni^{2+} in $LaNiO_{2.5}$ to metallic Ni [37]. The results are consistent with the XRD results that LNO perovskite structure was completely destroyed to Ni/La_2O_3 after reduction in H_2 at 700 ^oC for 1h.

Differently from the LNO profile, Ni/La_2O_3 profile shows another obvious peak at around 440 ^oC. It was caused by the reduction of Ni^{2+} in a nickel oxide phase (NiO) to Ni^0 [38], which was also detected in the XRD results. In addition, the first reduction peak of Ni^{3+} to Ni^{2+} was slightly shifted to higher temperatures for Ni/La_2O_3, which suggested a lower Ni dispersion of Ni/La_2O_3 than LNO. Previous studies also reported that Ni was homogeneously distributed in the LNO structure, which resulted in a highly dispersed Ni supported on La_2O_3 after reduction [39].

The substitution of partial La in LNO with Sr also resulted in the appearance of a new reduction peak at around 440 ^oC which should be assigned to the reduction peak of NiO to Ni^0. The presence of NiO in LSNO was also confirmed by the XRD results. In addition, the peak related to the reduction of Ni^{2+} in $LaNiO_{2.5}$ to Ni^0 in LSNO was shifted higher temperature to 610 ^oC compared with LNO. It should be explained by that the partial replacement of La by Sr increased the basicity of support and thus led to a stronger interaction between active metal and support [7].

As can be seen clearly in LSNFO, the addition of the secondary Fe component significantly affected the reducibility of monometallic Ni catalysts [4]. The first peak of Ni^{3+} to Ni^{2+} was shifted to lower temperature of 330 ^oC with the substitution of Fe in the B-site, implying the highest reducibility and dispersion of Ni in LSNFO. In this case, the presence of Fe provided extra oxygen

mobility due to the inherent redox properties of Fe, which promoted the reduction of Ni. The intensity of peaks at low temperature was much smaller than that for the other catalysts, implying the difficulty of completely reducing LSNFO at low temperature [23]. The second peak was shifted towards higher temperature of 510 ^{o}C compared with LSNO. This peak should be assigned to the reduction of strongly interacted iron with support with the aid of Ni, resulting the formation of Ni-Fe alloy, which was also confirmed by the XRD results. The third broad peak at temperature of higher than 900 ^{o}C should be associated with the reduction of Fe species strongly incorporated in the LSFO perovskite structure, which is difficult to be reduced at temperatures of < 900 ^{o}C. The low reducibility of LSFO was confirmed by the H_2-TPR result. Only a small reduction peak could be observed at 350 ^{o}C, which should be attributed to the reduction of high-valent Fe ions to Fe^{3+}. The lack of other reduction peaks before 700 ^{o}C indicated that most perovskite structures were remained after reduction, which provided more oxygen vacancies for the selective conversion of CO_2 to CO.

The dispersion of Ni in different catalysts, confirmed by the H_2-chemisportion analysis, followed an order of LSNFO > LSNO > LNO > Ni/La_2O_3 (**Table 1**), which was consistent with the results of H_2-TPR. It can be observed from **Table 1** that catalysts with weaker metal-support interaction (Ni/La_2O_3 and LNO) generally showed larger particle size and lower dispersion, since the active metals were easier to be migrated and aggregated during reduction. In contract, the catalysts with stronger metal-support interaction (LSNO and LSNFO) preferred to form smaller particle size and higher metal dispersion after reduction. In addition, the particle size of Ni calculated based on the Ni dispersion followed an order of LSNFO < LSNO < LNO < Ni/La_2O_3 (**Table 1**), which was consistent with that determined by XRD and TEM results.

Table 1 shows the H_2 uptake for the reduction of catalysts up to 700 ^{o}C and the reduction extend of active metals in different catalysts. The H_2 consumptions of Ni/La_2O_3, LNO, LSNO, LSFO and LSNFO were 4.02, 3.94, 4.06, 0.39 and 2.32 mmol/g, respectively, and the corresponding Ni- or Fe-based reduction extends were 101.2, 96.8, 97.6, 6.2 and 111.0%. It can be observed that Ni in the catalysts was almost completely reduced for all catalysts, indicating the reduction temperature of 700 ^{o}C was crucial to obtain reduced catalysts with most activated Ni species. In addition, the Ni-based reduction degree was more than 100% for LSNFO, and the excess H_2 should be related to the

reduction of Fe [23]. Hence, partial Fe in LSNFO was reduced as a Ni-rich Ni-Fe alloy, which was also evidenced by the XRD results in **Fig. 1(a-c)**.

3.1.3 FESEM and TEM analysis

The SEM morphologies of the reduced catalysts are shown in **Fig. 2**. Even though Ni/La_2O_3, LNO and LSNO showed similar XRD patterns in **Fig. 1(a-c)**, their morphologies were significantly different. The impregnated Ni/La_2O_3 catalyst shows a dense structure with irregular particles, which should be caused by the migration and aggregation of particles during reduction. However, the LNO, LSNO, LSFO and LSNFO catalysts were composed of uniform small particles in a loose structure, suggesting that perovskite structure was a promising precursor for the achievement of uniform and dispersed active metals on the support [40]. In addition, abundant pores can be observed in reduced LNO, LSNO, LSFO and LSNFO, which was caused by the accumulation of particles.

Figs. 3 (a-e) show that all reduced catalysts possessed rich metal particles except for LSFO. The lack of metallic Fe in reduced LSFO confirmed that most Fe was incorporated in the LSFO perovskite structure, which was in good agreement with the XRD and H_2-TPR results. In addition, it can be seen that Ni/La_2O_3 exhibited a larger Ni particle size and lower Ni dispersion compared with other catalysts. The metal particle size of Ni/La_2O_3, LNO, LSNO and LSNFO was 23.2, 16.3, 13.1 and 9.9 nm, respectively, which was consistent with the order of particle size determined by the XRD results. The smallest particle size of LSNFO should be attributed to the strongest metal-support interaction (as demonstrated in the TPR results) [23]. The distribution of active metals in the reduced LSNFO catalyst was confirmed using the TEM-EDX mapping, as presented in **Figs. 3 (f)**. The relative intensities of different elements clearly reflected their actual content in the catalyst. In addition, it can be seen that Ni and Fe were highly distributed in the catalyst and showed the same distribution, indicating the strong interaction between Ni and Fe to form a Ni-Fe alloy [41].

3.1.4 Textual analysis

The specific surface area and volume structure of calcined and reduced catalysts are presented in **Table 1**. Both the surface area and pore volume were increased after reduction, since more reduced metal particles with smaller particle size were exposed after reduction. In addition, it can be observed from **Fig. 2** that the particles might recombine to form new piled pores during reduction,

which also contributed to higher pore volume. Ni/La_2O_3 catalyst shows lower surface area and pore volume than LNO due to the easier aggregation of Ni particles for impregnated catalysts [42], which was in agreement with the FESEM result. Both the surface area and pore volume of reduced LSNO were lower than that of the reduced LNO, which might be caused by the deposition of Sr species in the pores of catalyst. The incomplete reduction of Fe species and the possible incorporation of Fe in the pore structure of perovskite might contribute to the lower surface area and pore volume of LSNFO compared with LSNO.

3.1.5 O_2- and CO_2-TPD analysis

The mobility of lattice oxygen in the reduced catalysts was determined by O_2-TPD, as shown in **Fig. 4(a)**. Typically, two kinds of oxygen desorption peaks are observed, which can be designated as α-oxygen and β-oxygen. The α-oxygen at 300-600 ^oC should be assigned to the chemical adsorbed oxygen on the surface (O_2^-) and the β-oxygen at temperatures of > 600 ^oC is related to the oxygen adsorbed on oxygen vacancies (O^-). The β-oxygen is considered as one of the most important properties of perovskite catalysts related to their catalytic performance, since the desorption of β-oxygen reflects both the number of oxygen vacancies (active site) and the difficulty of regenerating oxygen vacancies [43]. In this study, β-oxygen is not observed for Ni/La_2O_3, indicating its negligible oxygen vacancies. LNO, LSNO, LSFO and LSNFO shows obvious desorption peaks of β-oxygen at 650-850 ^oC and the maximum intensity of β-oxygen was achieved by LSNFO. In addition, the position of the β-oxygen was shifted to lower temperatures with the partial substitution of A sites and B sites, following an order of LSNFO < LSFO < LSNO < LNO. The result indicated the greatest oxygen storage capacity and highest oxygen mobility of LSNFO, which contributed to its superior catalytic performance for RWGS.

CO_2-TPD was performed in order to study the basicity of catalysts and the interaction of CO_2 and catalyst, as presented in **Fig. 4(b)**. According to the desorption temperature, three types of basic sites were recognized as the weak (50-230 ^oC), medium (230-700 ^oC) and strong basic sites (>700 ^oC). The weak basic sites should be attributed to the CO_2 desorption interacted with surface OH^-, moderate sites are produced by the low-coordination oxygen anions, and strong sites centered at 830-900 ^oC are related to the decomposition of bulk carbonate [44, 45]. It can be observed that the

peak intensity of moderate and strong basic sites for LSNO was much higher than other catalysts, due to the enhanced basicity with Sr doping. However, the Sr doped LSFO and LSNFO showed much lower peak intensities of moderate and strong basic sites. The reason should be that the Sr was still incorporated in the LSFO perovskite structure after reduction, resulting in its lower basicity than SrO. The weak basic sites are expected to primarily participate in the RWGS reaction since the reaction was conducted at low temperatures in DBD plasma [45]. It can be observed that LSNFO exhibited the highest intensity of weak adsorption sites, indicating its highest CO_2 adsorption capacity. In addition, the weak adsorption center of LSNFO was slightly shifted to higher temperatures, which suggested that the basic center in LSNFO was stronger compared with other catalysts [46]. The enhanced CO_2 adsorption capacity of LSNFO compared with LSNO and LSFO should be attributed to the formation of Ni-Fe alloy, where the presence of Fe as a redox promoter and the strong Ni-Fe interaction in Ni-Fe alloy enabled the electronically rich state of Ni atoms and facilitated the adsorption of CO_2 [4]. In addition, the abundant oxygen vacancies created by perovskite structure in LSFO and LSNFO provided more adsorption sites of CO_2 than LSNO, LNO and Ni/La_2O_3.

3.1.6 XPS analysis

The surface element states and compositions of reduced catalysts were measured by XPS. The deconvolution of O1s XPS spectra is displayed in **Fig. 5(a)**, in order to demonstrate the oxygen storage capacity and oxygen mobility of catalysts. Three oxygen species were identified by the deconvolution of O1s spectra for all catalysts. The first peak at around 528-529 eV should be assigned to the oxygen ions in the lattice oxygen. The second peak at around 530-531 eV was related to the adsorbed oxygen and the third peak at 532-533 eV should be attributed to the presence of adsorbed water [47]. It should be noted that the peak position of lattice oxygen for LSNFO was slightly shifted towards lower binding energy compared with the other catalysts, indicating the higher oxygen mobility of LSNFO [23]. The result should be explained by the lattice distortion caused by the Sr and Fe doping, which produced higher amounts of oxygen vacancies. Hence, the activation energy of lattice oxygen migrating was reduced and the lattice oxygen mobility was improved.

The ratio of different oxygen species was quantitatively analyzed, as shown in **Table 2**. It can be observed that the ratio of lattice oxygen for Ni/La_2O_3, LNO, LSNO, LSFO and LSNFO catalysts was 7.30, 8.78, 10.22, 17.31 and 33.05%, respectively. The higher concentration of lattice oxygen in LSNFO should be attributed to the remaining perovskite structure, which provided more oxygen vacancies and higher oxygen storage ability for LSNFO. In addition, LSFO also exhibited lower ratio of oxygen vacancies than LSNFO, which might be attributed to the high oxygen affinity of Fe, leading to the higher ratio of adsorption oxygen in LSFO. The higher oxygen storage ability and oxygen mobility in LSNFO was proven to enhance the adsorption of gas phase oxygen-containing species, such as CO_2 [7].

The Ni 2p spectra of all reduced catalysts were presented in **Fig. 5(b)**. Two Ni species were identified by deconvolution of Ni 2p spectra, which should be assigned to metallic Ni^0 at binding energy (B.E.) of 851~853 eV and Ni^{2+} at 855-857 eV [48]. Table 2 shows that Ni^0 was the main Ni species on the surface of reduced catalysts with ratio of 65-74%, which was consistent with the XRD results that Ni was almost completely reduced at 700 ^oC in H_2 for 1h. In addition, it should be noted that an obvious shift of Ni^0 B.E. towards lower value of 851.66 eV can be observed in the Ni 2p spectrum of LSNFO, which indicated the interaction between Ni and Fe by forming Ni-Fe alloy [35]. In addition, the Ni electronic environment might be affected in the presence of Fe, which resulted in an electronically richer state of Ni compared with the other catalysts and contributed to a higher catalytic performance of LSNFO [4].

3.1.7 XANES and EXAFS analysis

Figs. 6 (a, b) shows the normalized XANES spectra for the Ni and Fe K absorption edge for the reduced LSNFO sample and standard Ni and Fe foil and oxides. The XANES signals were extracted from the measured X-ray absorption spectra via the pre-edge background and were normalized by dividing the peak intensity by the height of the absorption edge. The data was analyzed by the Athena software. For the reduced LSNFO sample, the Ni K-edge XANES spectra (**Fig. 6a**) is very similar to that of metallic Ni foil, with no significant white line intensity and a prominent pre-edge peak. This shows that Ni was almost completely reduced to metallic state in the reduced LSNFO

sample [49]. For the Fe-edge (**Fig 6b**), the XANES spectra of the reduced LSNFO sample presents a white line intensity which is higher than that of metallic Fe foil but lower than that of Fe^{2+} and Fe^{3+} (FeO and Fe_2O_3 standards). Since XAS is a bulk technique, this implies that after reduction, part of the Fe in LSFNO existed in metallic state and part of it was still in oxidized state. This is supported by the XRD results of the reduced LSNFO sample, which shows peaks for LSFO perovskite phase in addition to metallic Ni-Fe alloy in the reduced LSNFO catalyst. The remaining of partial LSFO perovskite structure enhanced the formation of CO by increasing oxygen storage capacity and oxygen mobility.

EXAFS experiments at the Ni and Fe K-edge were performed on the reduced LSNFO catalyst to investigate the local coordination structure of Ni and Fe and to confirm the formation of a Ni-Fe alloy phase. **Fig. 6(c)** shows the magnitude of the Fourier Transform (FT) of Ni and Fe edge EXAFS data of reduced LSNFO, LNO and reference Ni and Fe foils. It is clearly observed that the Ni edge spectra for both the LSNFO and LNO samples followed the pattern of reference Ni foil, corresponding to metallic nickel with an fcc crystal structure. On the other hand, the standard Fe foil showed a spectra pattern corresponding to a bcc crystal structure. It is interesting to note that the peaks in the FT of Fe edge EXAFS of reduced LSNFO corresponding to the higher order Fe-Fe(Ni) coordination shells (3-6 Å) followed the fcc crystal structure of Ni foil instead of the bcc structure of Fe foil. This shows that Fe formed a homogenous alloy with Ni instead of a separate Fe phase, which contributed to the superior performance of LSNFO by generating a synergistic effect.

3.2 Catalytic performance and stability

3.2.1 RWGS activity

The activity of Ni/La_2O_3, LNO, LSNO, LSFO and LSNFO catalysts was tested and compared for RWGS reaction with a H_2/CO ratio of 1:1 in DBD plasma at low temperature and atmospheric pressure. In addition, the performance of RWGS in plasma-only and thermal-catalysis system was also studied as a reference in order to show the advantage of NTP-catalysis system.

Figs. 7(a)-(c) shows the conversion of CO_2, and selectivity of CO and CH_4 in plasma-only and hybrid plasma-catalysis system over impregnated Ni/La_2O_3, and LNO, LSNO, LSFO and LSNFO perovskites at 35-120 ^oC. At such low temperatures, the activity of catalysts was negligible due to the

thermodynamic limitation and the RWGS reaction can only be initialed in the presence of plasma, in spite of the use of catalysts. The plasma-only system without any catalysts showed low CO_2 conversion and CO selectivity. The addition of LSFO in the discharge gap of DBD plasma did not increase CO_2 conversion, suggesting the poor activity of LSFO on C=O activation and CO_2 conversion. However, a much higher selectivity of CO was achieved due to the redox property and more oxygen vacancies of Fe-containing catalyst. The integration of Ni-based catalysts in DBD plasma promoted the conversion of CO_2 to CO efficiently in the hybrid plasma-catalysis system and the catalytic activity of different catalysts decreases by an order of LSNFO > LSNO > LNO > Ni/La_2O_3. Even though Ni/La_2O_3 had the same Ni loading ratio and even similar XRD patterns for the reduced catalysts with LNO perovskite, LNO exhibited higher activity in terms of CO_2 conversion and CO selectivity. It should be attributed to the higher dispersion of Ni^0 on the support (La_2O_3) [39] and the smaller Ni particle size for LNO, evidenced by TEM images (**Fig. 3**) and H_2-chemisorption results (**Table 1)**. In addition, the higher selectivity of CO and lower selectivity of CH_4 over LNO should also be attributed to the higher concentration of lattice oxygen and oxygen vacancies (**Fig. 4a, Fig. 5** and **Table 2**) which promoted the selective conversion of CO_2 to CO [21]. LSNO showed higher activity than LNO with increasing the selectivity of CO from 26-52% to 31-64%, and decreasing the selectivity of CH_4 from 0.5-17% to 0.4-9%. Doping of Sr was proven to increase the concentration of oxygen vacancies and mobility of active oxygen of catalysts confirmed by the XPS results, leading to enhanced adsorption of oxygen species in the gaseous phase [23]. In addition, the increased basicity of Sr-doped LNO as shown in **Fig. 4(b)** also contributed to the promoted formation of CO and suppressed formation of CH_4 [7]. The conversion of CO_2 slightly decreased from 34-57% to 33-56% by doping of Sr, since the doping of Sr suppressed the methane formation. The further doping of Fe in the B site of LSNO resulted in the highest activity of LSNFO with the maximum CO selectivity of 33-85%, and the minimum CH_4 selectivity of 0.3-4%.

The superior catalytic performance of LSNFO should be explained as follows. The doping of Fe with a Ni/Fe molar ratio of 1:1 favored the intimate interaction between Ni and Fe to form Ni-Fe alloy after reduction of LSNFO. Therefore, higher dispersion and smaller size of metal particles, stronger metal-support interactions and electronically rich state of Ni atoms could be achieved,

which promoted the adsorption and conversion of CO_2 [7]. At the same time, the redox properties of Fe played an important role in enhancing the selective formation of CO and suppressing the competitive Sabatier (CO_2 methanation) reaction by providing extra oxygen mobility [4]. In addition, the strong interaction between Fe and La in LSNFO made it difficult to be completely reduced at 700 ^oC, and particle Fe was remained in the LSFO perovskite phase, which was evidenced by the XRD and XAS results. The presence of LSFO perovskite structure in the reduced LSNFO catalyst could supply much more oxygen vacancies and increase the mobility of active oxygen, as confirmed by the XPS results. As a result, the adsorption of CO_2 and selective conversion of CO_2 to CO was enhanced via redox mechanism, in which oxygen vacancies played the most crucial role for RWGS [21]. The outstanding performance of DBD plasma-LSNFO hybrid system also proved that the Ni-Fe alloy and oxygen vacancies in LSNFO can be activated in plasma even at low temperatures, which promoted the adsorption and reaction of highly active species and electrons generated by plasma [50].

The conversion of CO_2 increased with increase of discharge power for all the catalysts. However, they showed different behavior for the selectivity of CO and CH_4. The selectivity of CO increased initially with the increase in discharge power from 10 to 49 W, while decreased sharply with a further increase of discharge power to 89 W for Ni/La_2O_3 and LNO catalysts. Simultaneously, a dramatic increase was observed for the selectivity of CH_4 after 49 W, due to the high activity of Ni towards an undesirable side reaction of CO_2 methanation. At lower discharge power, the C=O bonds in CO_2 with a binding energy of 8.3 eV was decomposed to produce CO and O radical in DBD plasma (Eq. 7). The produced O radical reacted with H_2 to generate H_2O (Eq. 9). At higher discharge power, the dissociation of C≡O in CO with a higher binding energy of 11.1 eV was enhanced in the gas phase (Eq. 8), and subsequently CH_4 was formed from the recombination of the obtained C and H_2 via Eq. (10). The formation of CH_4 was significantly suppressed over LSNO due to the addition of alkaline metals Sr. However, the sharp increase of CH_4 selectivity could still be observed at 89 W. Different from the other three catalysts, the selectivity of CO increased continuously with the increase of discharge power over LSNFO, and simultaneously the selectivity of CH_4 was suppressed efficiently, indicating the superior performance of LSNFO for RWGS.

The carbon balance of RWGS over different catalysts was calculated based on the production of CO and CH_4, as displayed in Fig. **7(d)**. It can be observed that the carbon balance over different catalysts increased with the discharge powers and it achieved the highest value of 90% over LSNFO at 89 W. It should be noted that the carbon balance was less than 100%, especially at lower discharge powers, since multiple reaction pathways occurred concurrently with generating a variety of byproducts in plasma. The mass spectrometry (MS) analysis of the products revealed that more byproducts such as methanol, ethanol and C2-C3 hydrocarbons would be produced at lower discharge powers since the combination of reactants and radicals was preferred at lower discharge powers, while the decomposition reactions was dominant at higher discharge power (**Fig. S3**) [51]. The detail analysis was presented in the *electronic supplementary information (ESI)*.

$$CO_2 \rightarrow CO + O \quad (7)$$

$$CO \rightarrow C + O \quad (8)$$

$$O + H_2 \rightarrow H_2O \quad (9)$$

$$C + 2H_2 \rightarrow CH_4 \quad (10)$$

The performance of RWGS reaction in thermal catalysis system was also tested at 400-600 ^oC over LSNFO and compared with that in plasma-catalysis system, as shown in **Fig. 7(e)**. The CO_2 conversion achieved the maximum of 40% at 600 ^oC, which was much lower than the 56% obtained in the plasma-catalysis system at 89 W over the same catalyst. In addition, the selectivity of CO at 600 ^oC was 90%, close to the 84% which achieved in plasma-catalysis system. By comparison, therefore, the superior potential of the DBD plasma-catalysis system can be recognized in activating the perovskite catalysts and promote the RWGS reactions at low temperature, which opens up a new sight and possibility for the enablement of some thermodynamically unfavorable reactions or high temperature and high pressure reactions.

3.2.2 Effect of H_2/CO_2 ratio

The effect of H_2/CO_2 ratio on the performance of LSNFO was investigated by varying the H_2/CO_2 ratio from 4:1 to 1:4, in order to optimize the condition of RWGS with a maximum CO_2 conversion and CO selectivity. The obtained results are depicted in **Figs. 8(a)-(d)**. The conversion of CO_2 increased with the increasing H_2/CO_2 ratio, since a H_2 feed higher than the stoichiometric

concentration of RWGS promoted the conversion of CO_2. The maximum conversion of CO_2 was achieved with a H_2/CO_2 ratio of 4:1. However, the minimum selectivity of CO was obtained as well as the maximum CH_4 selectivity, since a H_2/CO_2 ratio of 4:1 promoted the reaction of CO_2 methanation as Eq. (11). Previous studies reported that the selectivity of CH_4 could reach high values of >90% in DBD plasma with a H_2/CO_2 ratio of 4:1 over Ni-based catalysts [52]. However, the selectivity of CH_4 is lower than 45% even with a H_2/CO_2 ratio of 4:1 in this study. The differences should be explained by the redox potential of Fe, which favors the selective formation of CO [35], whereas, Ni was evidenced to be more reactive in the production of CH_4 [53]. A low H_2/CO_2 ratio of 1:2 and 1:4 contributed to the much higher selectivity of CO (nearly 100%), while the conversion of CO_2 was significantly reduced, leading to the lower yield of CO (**Fig. 8d**). Both higher CO_2 conversion and higher CO selectivity was showed with a H_2/CO_2 ratio of 2:1 compared with that with a stoichiometric H_2/CO_2 ratio of 1:1 for RWGS. A higher H_2 concentration accelerated the extraction of lattice oxygen adsorbed in the oxygen vacancies of LSNFO [54], and consequently provided more reactive site for the further dissociation of CO_2 to CO. As a consequence, a H_2/CO_2 ratio of 2:1 was the most favorable for the RWGS with the highest CO yield.

$$4H_2 + CO_2 \rightarrow CH_4 + 2H_2O \quad (11)$$

3.2.3 Stability of LSNFO

The stability of LSNFO for RWGS with a H_2/CO ratio of 2:1 was investigated, since the possible carbon formation via reaction (6) and catalyst agglomeration could lead to the deactivation of LSNFO. **Fig. S4** shows that the LSNFO was quite stable for the RWGS reaction after 100 h. The conversion of CO_2 was maintained constantly at ~60%, with CO selectivity of ~90% and CH_4 selectivity of ~10%. In addition, TG-DTA analysis was conducted to show the amount and nature of coke deposition on the spent LSNFO after 100h stability test, as shown in **Fig. S5**. The TG-DTA profiles show an obvious exothermic mass gain at 170-400 ^oC which should be attributed to the oxidation of Ni-Fe species, and an exothermic mass loss at 400-800 ^oC which should be assigned to the oxidation of coke. The formation rate of coke on LSNFO is only 0.2 mgC/(gCat·h), which also confirmed the outstanding coke resistance ability of LSNFO [46]. The mechanism of RWGS in hybrid plasma-catalysis system and the interactions between plasma and catalysts was complex due

to the co-existence of various highly reactive species and energetic electrons and the lack of *in situ* characterization instrument [50]. The possible mechanism of RWGS over LNO and LSNFO was hypothesized (Fig. S8) based on the on-line FTIR analysis of gas products (Figs. S6 and S7) and *ex situ* ATR analysis of catalysts (Fig. S9). More efforts are necessary for demonstrating the real-time mechanism of plasma-catalysis reactions by developing more advanced *in situ* characterization methods in the future.

The performance of RWGS in the hybrid DBD plasma-catalysis system was evaluated and compared with other state-of-the-art catalysis systems, as presented in **Table 3**. Different catalysts including Mo_2C supported Co [55] and Cu [1], Al_2O_3-supported Fe [56], Ni-Fe [4] and Fe-Cu [57], and even some noble metals of Ir [11], Pt [13] and Au [21] have been employed in the RWGS in thermal-catalysis system, which generally showed high CO selectivity of >70% [55, 58]. However, the conversion of CO_2 in most cases remained lower than 50% even at high temperatures due to the unfavorable thermodynamic barrier. Yang et al. [4] found that temperatures of above 600 ^oC favored RWGS reaction over Ni-Fe_2O_3/CeO_2-Al_2O_3, while a lower temperature range (400-600 ^oC) promoted the CO_2 methanation significantly. NTP was generally operated at low temperature, which reduced the risk of catalyst deactivation caused by sintering and agglomeration. However, the plasma-only system exhibited a low CO selectivity of 54% in this study due to the formation of undesirable byproducts, such as CH_4 and carbon. Wang et al. [51] employed Cu/γ-Al_2O_3 catalyst for the synthesis of methanol from H_2 and CO_2 with a ratio of 3:1 in a modified DBD plasma reactor. A selectivity of ~40% towards CO formation was achieved together with a CO_2 conversion of 21.1%. In this study, the hybrid DBD plasma-LSNFO perovskite catalyst system showed a remarkable performance, which achieved both high CO_2 conversion (60%) and high CO selectivity (90%) simultaneously for a long-term stability test of 100 h at low temperature and atmospheric pressure. The TOF value of LSNFO in DBD plasma-catalysis system was at a moderate level of 0.21 s^{-1} among all catalysts listed in **Table 3**. Specifically, previous studies showed that much higher TOF values were achieved over Cu/β-Mo_2C (3.7 s^{-1}) [1] and K_{80}-Pt/L (2.25 s^{-1}) [13] in thermal-catalysis system, however, much higher temperatures of > 500 ^oC are required even over noble metal catalyst of K_{80}-Pt/L. The lower TOF value of LSNFO should be attributed to the higher metal loading which

was determined by the stoichiometric ratio of perovskites. Further optimization of the operation parameters such as the feed gas flowrate and gas hourly space velocity should be studied, in order to increase the TOF values.

4. Conclusion

The reverse water-gas shift (RWGS) reaction was investigated over a hybrid dielectric barrier discharge (DBD) plasma-catalysis process. $La_{0.9}Sr_{0.1}Ni_{0.5}Fe_{0.5}O_{3+\delta}$ (LSNFO) catalyst shows the most potential in the selective conversion of CO_2 to CO and the suppression of CH_4 formation, compared with $LaNiO_3$ (LNO), $La_{0.9}Sr_{0.1}NiO_{3+\delta}$ (LSNO) and impregnated Ni/La_2O_3 catalysts. The superior catalytic performance of LSNFO is attributed to the formation of uniform Ni-Fe alloys and presence of residual perovskite structures. On one hand, Ni and Fe generate a synergistic effect by the formation of uniform Ni-Fe alloy and promote the dissociation of H_2. On the other hand, the residual LSFO perovskite structure in LSNFO catalyst favors to provide greater amount of oxygen vacancies and results in a higher oxygen mobility, which promotes the adsorption and dissociation of CO_2. In addition, on account of the different performance between LSNFO and other catalysts, two mechanisms are proposed. The redox mechanism plays a crucial role in the RWGS reaction over LSNFO catalyst and the associated formate mechanism dominates the RWGS reaction over LNO catalyst.

Author Contributions

L. Liu conceived the idea, designed the DBD plasma-catalysis reactor, carried out the catalytic tests, did the catalyst characterizations using N_2 adsorption-desorption, XRD, FESEM, TEM, H_2-TPR, CO_2-TPD, O_2-TPD and XPS, analyzed the data and wrote the manuscript under the guidance of S. Kawi. S. Das did the analysis of XANES and EXAFS data and wrote the XANES and EXAFS part. T. Chen helped synthesize the catalysts and do XRD, FESEM and TEM analysis. N. Dewangan helped do the ATR and FTIR characterization and analyze the ATR and FTIR data. J. Ashok did the thermal catalysis experiment over LSNFO. S. Xi and A. Borgna did the XANES and EXAFS experiments. Z. Li helped drew the graphic abstract.

Declaration of Interest Statement

There is no conflict of interest.

5. Acknowledgement

The research is financially supported by National Environmental Agency (NEA-ETRP Grant 1501 103, WBS No. R-279-000-491-279), A*STAR (AME-IRG A1783c0016, WBS No. R-279-000-509-305) and Ministry of Education (MOE2017-T2-2-130, WBS No. R-279-000-544-112).

References

[1] X. Zhang, X. Zhu, L. Lin, S. Yao, M. Zhang, X. Liu, X. Wang, Y. Li, C. Shi, D. Ma, Highly dispersed copper over β-Mo_2C as an efficient and stable catalyst for the reverse water gas shift (RWGS) reaction, ACS Catalysis, 7 (2016) 912-918.

[2] Z. Bian, I.Y. Suryawinata, S. Kawi, Highly carbon resistant multicore-shell catalyst derived from Ni-Mg phyllosilicate nanotubes@silica for dry reforming of methane, Applied Catalysis B: Environmental, 195 (2016) 1-8.

[3] M. Roiaz, E. Monachino, C. Dri, M. Greiner, A. Knop-Gericke, R. Schlögl, G. Comelli, E. Vesselli, Reverse water–gas shift or Sabatier methanation on Ni (110)? Stable surface species at near-ambient pressure, Journal of the American Chemical Society, 138 (2016) 4146-4154.

[4] L. Yang, L. Pastor-Pérez, S. Gu, A. Sepúlveda-Escribano, T. Reina, Highly efficient Ni/CeO_2-Al_2O_3 catalysts for CO_2 upgrading via reverse water-gas shift: Effect of selected transition metal promoters, Applied Catalysis B: Environmental, 232 (2018) 464-471.

[5] W. Wang, Y. Himeda, J.T. Muckerman, G.F. Manbeck, E. Fujita, CO_2 hydrogenation to formate and methanol as an alternative to photo-and electrochemical CO_2 reduction, Chemical Reviews, 115 (2015) 12936-12973.

[6] C.Á. Galván, J. Schumann, M. Behrens, J.L.G. Fierro, R. Schlögl, E. Frei, Reverse water-gas shift reaction at the Cu/ZnO interface: influence of the Cu/Zn ratio on structure-activity correlations, Applied Catalysis B: Environmental, 195 (2016) 104-111.

[7] Z. Zhang, L. Liu, B. Shen, C. Wu, Preparation, modification and development of Ni-based catalysts for catalytic reforming of tar produced from biomass gasification, Renewable and Sustainable Energy Reviews, 94 (2018) 1086-1109.

[8] Z. Li, M. Li, Z. Bian, Y. Kathiraser, S. Kawi, Design of highly stable and selective core/yolk–shell nanocatalysts—A review, Applied Catalysis B: Environmental, 188 (2016) 324-341.

[9] M.D. Porosoff, B. Yan, J.G. Chen, Catalytic reduction of CO_2 by H_2 for synthesis of CO, methanol and hydrocarbons: challenges and opportunities, Energy & Environmental Science, 9 (2016) 62-73.

[10] K. Oshima, T. Shinagawa, Y. Nogami, R. Manabe, S. Ogo, Y. Sekine, Low temperature catalytic reverse water gas shift reaction assisted by an electric field, Catalysis Today, 232 (2014) 27-32.

[11] X. Chen, X. Su, H. Su, X. Liu, S. Miao, Y. Zhao, K. Sun, Y. Huang, T. Zhang, Theoretical insights and the corresponding construction of supported metal catalysts for highly selective CO_2 to CO conversion, ACS Catalysis, 7 (2017) 4613-4620.

[12] M. Yang, L.F. Allard, M. Flytzani-Stephanopoulos, Atomically dispersed Au–$(OH)_x$ species bound on titania catalyze the low-temperature water-gas shift reaction, Journal of the American Chemical Society, 135 (2013) 3768-3771.

[13] X. Yang, X. Su, X. Chen, H. Duan, B. Liang, Q. Liu, X. Liu, Y. Ren, Y. Huang, T. Zhang, Promotion effects of potassium on the activity and selectivity of Pt/zeolite catalysts for reverse water gas shift reaction, Applied Catalysis B: Environmental, 216 (2017) 95-105.

[14] Q. Zhang, L. Pastor-Pérez, W. Jin, S. Gu, T. Reina, Understanding the promoter effect of Cu and Cs over highly effective β-Mo_2C catalysts for the reverse water-gas shift reaction, Applied Catalysis B: Environmental, 244 (2019) 889-898.

[15] M.D. Porosoff, J.G. Chen, Trends in the catalytic reduction of CO_2 by hydrogen over supported monometallic and bimetallic catalysts, Journal of Catalysis, 301 (2013) 30-37.

[16] H. Yue, Y. Zhao, S. Zhao, B. Wang, X. Ma, J. Gong, A copper-phyllosilicate core-sheath nanoreactor for carbon–oxygen hydrogenolysis reactions, Nature Communications, 4 (2013) 2339.
[17] Y. Zeng, L. Wang, C. Wu, J. Wang, B. Shen, X. Tu, Low temperature reforming of biogas over K-, Mg-and Ce-promoted Ni/Al_2O_3 catalysts for the production of hydrogen rich syngas: Understanding the plasma-catalytic synergy, Applied Catalysis B: Environmental, 224 (2018) 469-478.
[18] L. Liu, Q. Wang, J. Song, S. Ahmad, X. Yang, Y. Sun, Plasma-assisted catalytic reforming of toluene to hydrogen rich syngas, Catalysis Science & Technology, 7 (2017) 4216-4231.
[19] X. Jia, X. Zhang, N. Rui, X. Hu, C. Liu, Structural effect of Ni/ZrO_2 catalyst on CO_2 methanation with enhanced activity, Applied Catalysis B: Environmental, 244 (2019) 159-169.
[20] G. Chen, V. Georgieva, T. Godfroid, R. Snyders, M.-P. Delplancke-Ogletree, Plasma assisted catalytic decomposition of CO_2, Applied Catalysis B: Environmental, 190 (2016) 115-124.
[21] L.F. Bobadilla, J.L. Santos, S. Ivanova, J.A. Odriozola, A. Urakawa, Unravelling the role of oxygen vacancies in the mechanism of the reverse water–gas shift reaction by operando DRIFTS and ultraviolet–visible spectroscopy, ACS Catalysis, 8 (2018) 7455-7467.
[22] S.S. Kim, H.H. Lee, S.C. Hong, The effect of the morphological characteristics of TiO_2 supports on the reverse water–gas shift reaction over Pt/TiO_2 catalysts, Applied Catalysis B: Environmental, 119 (2012) 100-108.
[23] U. Oemar, M. Ang, W. Hee, K. Hidajat, S. Kawi, Perovskite $LaxM_{1-x}Ni_{0.8}Fe_{0.2}O_3$ catalyst for steam reforming of toluene: Crucial role of alkaline earth metal at low steam condition, Applied Catalysis B: Environmental, 148 (2014) 231-242.
[24] D.H. Kim, J.L. Park, E.J. Park, Y.D. Kim, S. Uhm, Dopant effect of barium zirconate-based perovskite-type catalysts for the intermediate-temperature reverse water gas shift reaction, ACS Catalysis, 4 (2014) 3117-3122.
[25] Y.A. Daza, R.A. Kent, M.M. Yung, J.N. Kuhn, Carbon dioxide conversion by reverse water–gas shift chemical looping on perovskite-type oxides, Industrial & Engineering Chemistry Research, 53 (2014) 5828-5837.
[26] L. Liu, Y. Liu, J. Song, S. Ahmad, J. Liang, Y. Sun, Plasma-enhanced steam reforming of different model tar compounds over Ni-based fusion catalysts, Journal of Hazardous Materials, 377 (2019) 24-33.
[27] L. Liu, Z. Zhang, S. Das, S. Kawi, Reforming of tar from biomass gasification in a hybrid catalysis-plasma system: A review, Applied Catalysis B: Environmental, 250 (2019) 250-272.
[28] J. Van Durme, J. Dewulf, C. Leys, H. Van Langenhove, Combining non-thermal plasma with heterogeneous catalysis in waste gas treatment: A review, Applied Catalysis B: Environmental, 78 (2008) 324-333.
[29] B. Pietruszka, M. Heintze, Methane conversion at low temperature: the combined application of catalysis and non-equilibrium plasma, Catalysis Today, 90 (2004) 151-158.
[30] H.-H. Kim, S.-M. Oh, A. Ogata, S. Futamura, Decomposition of gas-phase benzene using plasma-driven catalyst (PDC) reactor packed with Ag/TiO_2 catalyst, Applied Catalysis B: Environmental, 56 (2005) 213-220.

[31] D. Mei, X. Zhu, C. Wu, B. Ashford, P.T. Williams, X. Tu, Plasma-photocatalytic conversion of CO2 at low temperatures: Understanding the synergistic effect of plasma-catalysis, Applied Catalysis B: Environmental, 182 (2016) 525-532.
[32] X. Zhu, S. Zhang, Y. Yang, C. Zheng, J. Zhou, X. Gao, X. Tu, Enhanced performance for plasma-catalytic oxidation of ethyl acetate over $La_{1-x}Ce_xCoO_{3+\delta}$ catalysts, Applied Catalysis B: Environmental, 213 (2017) 97-105.
[33] Y. Hu, M.F. Aygüler, M.L. Petrus, T. Bein, P. Docampo, Impact of rubidium and cesium cations on the moisture stability of multiple-cation mixed-halide perovskites, ACS Energy Letters, 2 (2017) 2212-2218.
[34] Y. Kathiraser, W. Thitsartarn, K. Sutthiumporn, S. Kawi, Inverse $NiAl_2O_4$ on $LaAlO_3$–Al_2O_3: unique catalytic structure for stable CO_2 reforming of methane, The Journal of Physical Chemistry C, 117 (2013) 8120-8130.
[35] J. Ashok, S. Kawi, Nickel–iron alloy supported over iron–alumina catalysts for steam reforming of biomass tar model compound, ACS Catalysis, 4 (2013) 289-301.
[36] S. Fang, Y. Xia, K. Lv, Q. Li, J. Sun, M. Li, Effect of carbon-dots modification on the structure and photocatalytic activity of g-C3N4, Applied Catalysis B: Environmental, 185 (2016) 225-232.
[37] X. Li, D. Li, H. Tian, L. Zeng, Z.-J. Zhao, J. Gong, Dry reforming of methane over Ni/La_2O_3 nanorod catalysts with stabilized Ni nanoparticles, Applied Catalysis B: Environmental, 202 (2017) 683-694.
[38] J. Ashok, Y. Kathiraser, M. Ang, S. Kawi, Bi-functional hydrotalcite-derived NiO–CaO–Al_2O_3 catalysts for steam reforming of biomass and/or tar model compound at low steam-to-carbon conditions, Applied Catalysis B: Environmental, 172 (2015) 116-128.
[39] M.M. Nair, S. Kaliaguine, F. Kleitz, Nanocast $LaNiO_3$ perovskites as precursors for the preparation of coke-resistant dry reforming catalysts, ACS Catalysis, 4 (2014) 3837-3846.
[40] R. Rabelo-Neto, H. Sales, C. Inocêncio, E. Varga, A. Oszko, A. Erdohelyi, F. Noronha, L. Mattos, CO_2 reforming of methane over supported $LaNiO_3$ perovskite-type oxides, Applied Catalysis B: Environmental, 221 (2018) 349-361.
[41] X. Zou, T. Chen, P. Zhang, D. Chen, J. He, Y. Dang, Z. Ma, Y. Chen, P. Toloueinia, C. Zhu, High catalytic performance of Fe-Ni/Palygorskite in the steam reforming of toluene for hydrogen production, Applied Energy, 226 (2018) 827-837.
[42] L. Mo, S. Kawi, An in situ self-assembled core–shell precursor route to prepare ultrasmall copper nanoparticles on silica catalysts, Journal of Materials Chemistry A, 2 (2014) 7837-7844.
[43] J. Zhu, H. Li, L. Zhong, P. Xiao, X. Xu, X. Yang, Z. Zhao, J. Li, Perovskite oxides: preparation, characterizations, and applications in heterogeneous catalysis, ACS Catalysis, 4 (2014) 2917-2940.
[44] W. Li, X. Nie, X. Jiang, A. Zhang, F. Ding, M. Liu, Z. Liu, X. Guo, C. Song, ZrO_2 support imparts superior activity and stability of Co catalysts for CO_2 methanation, Applied Catalysis B: Environmental, 220 (2018) 397-408.
[45] A. Quindimil, U. De-La-Torre, B. Pereda-Ayo, J.A. González-Marcos, J.R. González-Velasco, Ni catalysts with La as promoter supported over Y-and BETA-zeolites for CO2 methanation, Applied Catalysis B: Environmental, 238 (2018) 393-403.

[46] J. Ashok, S. Das, N. Dewangan, S. Kawi, H_2S and NO_x tolerance capability of CeO_2 doped $La_{1-x}Ce_xCo_{0.5}Ti_{0.5}O_{3-\delta}$ perovskites for steam reforming of biomass tar model reaction, Energy Conversion and Management: X, (2019) 100003.
[47] F. Liang, Y. Yu, W. Zhou, X. Xu, Z. Zhu, Highly defective CeO_2 as a promoter for efficient and stable water oxidation, Journal of Materials Chemistry A, 3 (2015) 634-640.
[48] R. Kavian, S.-I. Choi, J. Park, T. Liu, H.-C. Peng, N. Lu, J. Wang, M.J. Kim, Y. Xia, S.W. Lee, Pt–Ni octahedral nanocrystals as a class of highly active electrocatalysts toward the hydrogen evolution reaction in an alkaline electrolyte, Journal of materials Chemistry A, 4 (2016) 12392-12397.
[49] S. Das, J. Ashok, Z. Bian, N. Dewangan, M. Wai, Y. Du, A. Borgna, K. Hidajat, S. Kawi, Silica–Ceria sandwiched Ni core–shell catalyst for low temperature dry reforming of biogas: Coke resistance and mechanistic insights, Applied Catalysis B: Environmental, 230 (2018) 220-236.
[50] S. Xu, S. Chansai, C. Stere, B. Inceesungvorn, A. Goguet, K. Wangkawong, S.R. Taylor, N. Al-Janabi, C. Hardacre, P.A. Martin, X. Fan, Sustaining metal–organic frameworks for water–gas shift catalysis by non-thermal plasma, Nature Catalysis, 2 (2019) 142.
[51] L. Wang, Y. Yi, H. Guo, X. Tu, Atmospheric pressure and room temperature synthesis of methanol through plasma-catalytic hydrogenation of CO_2, ACS Catalysis, 8 (2017) 90-100.
[52] E. Jwa, S. Lee, H. Lee, Y. Mok, Plasma-assisted catalytic methanation of CO and CO_2 over Ni–zeolite catalysts, Fuel Processing Technology, 108 (2013) 89-93.
[53] G. Garbarino, C. Wang, T. Cavattoni, E. Finocchio, P. Riani, M. Flytzani-Stephanopoulos, G. Busca, A study of Ni/La-Al_2O_3 catalysts: A competitive system for CO_2 methanation, Applied Catalysis B: Environmental, 248 (2019) 286-297.
[54] H. Sun, J. Wang, J. Zhao, B. Shen, J. Shi, J. Huang, C. Wu, Dual functional catalytic materials of Ni over Ce-modified CaO sorbents for integrated CO_2 capture and conversion, Applied Catalysis B: Environmental, 244 (2019) 63-75.
[55] M.D. Porosoff, X. Yang, J.A. Boscoboinik, J.G. Chen, Molybdenum carbide as alternative catalysts to precious metals for highly selective reduction of CO_2 to CO, Angewandte Chemie International Edition, 53 (2014) 6705-6709.
[56] L. Pastor-Pérez, M. Shah, E. Le Saché, T. Ramirez Reina, Improving Fe/Al_2O_3 catalysts for the reverse water-gas shift reaction: on the effect of Cs as activity/selectivity promoter, Catalysts, 8 (2018) 608.
[57] L. Pastor-Pérez, F. Baibars, E. Le Sache, H. Arellano-Garcia, S. Gu, T. Ramirez Reina, CO_2 valorisation via reverse water-gas shift reaction using advanced Cs doped Fe-Cu/Al_2O_3 catalysts, Journal of CO_2 Utilization, 21 (2017) 423-428.
[58] M. Ronda-Lloret, S. Rico-Francés, A. Sepúlveda-Escribano, E.V. Ramos-Fernandez, CuO_x/CeO_2 catalyst derived from metal organic framework for reverse water-gas shift reaction, Applied Catalysis A: General, 562 (2018) 28-36.

Figure Captions

Fig. 1. XRD patterns of (a) fresh and (b-c) reduced Ni/La_2O_3, LNO, LSNO, LSFO and LSNFO catalysts (▼perovskite, ◆La_2O_3,▽metallic Ni,◇ Ni-rich Ni-Fe alloy, ● NiO); (d) H_2-TPR profile of Ni/La_2O_3, LNO, LSNO, LSFO and LSNFO catalysts.

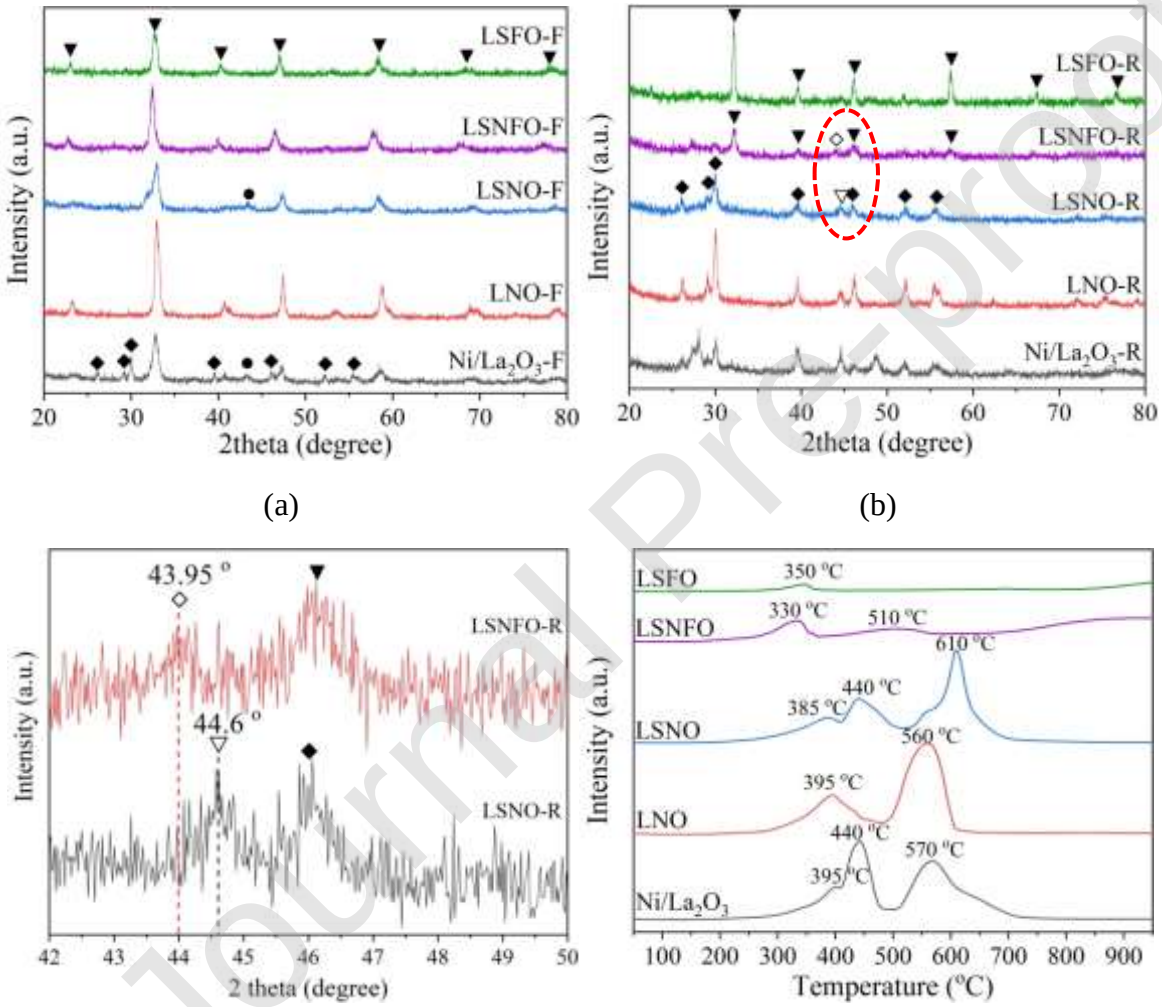

Fig. 1.

Fig. 2. FESEM images of reduced (a) Ni/La_2O_3, (b) LNO, (c) LSNO, (d) LSFO and (e) LSNFO.

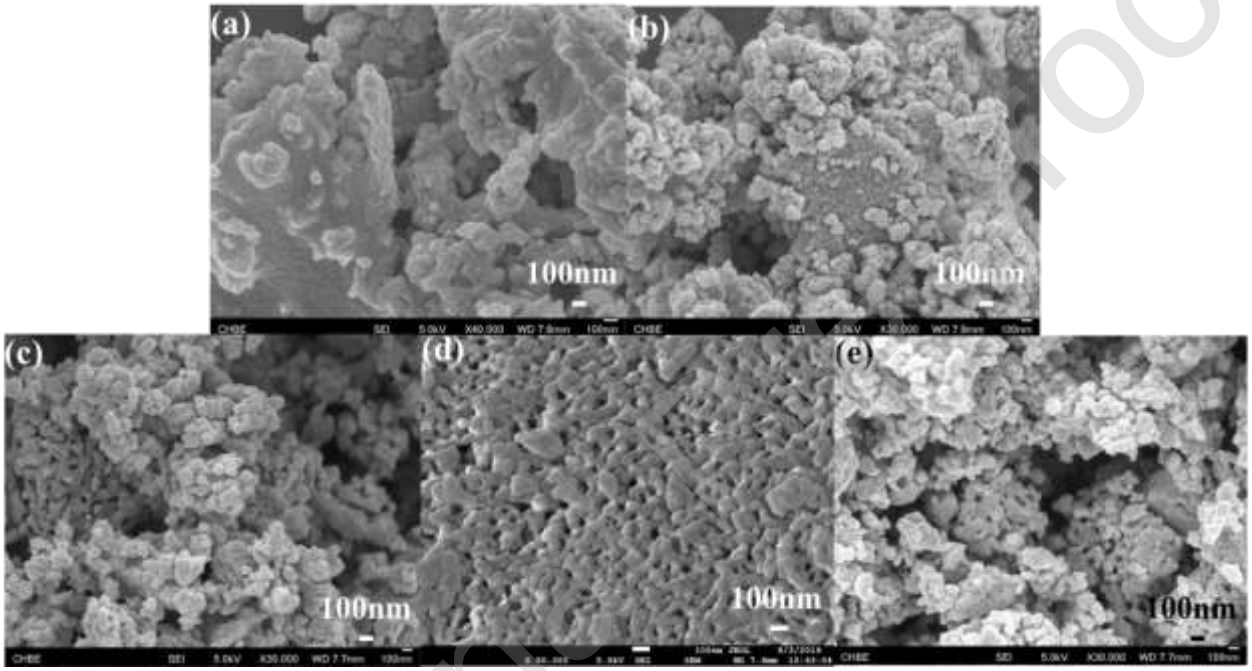

Fig. 2.

Fig. 3. TEM images of reduced (a) Ni/La_2O_3, (b) LNO, (c) LSNO, (d) LSFO, (e) LSNFO, and (f) element mapping of La, Sr, Ni, Fe and O for LSNFO.

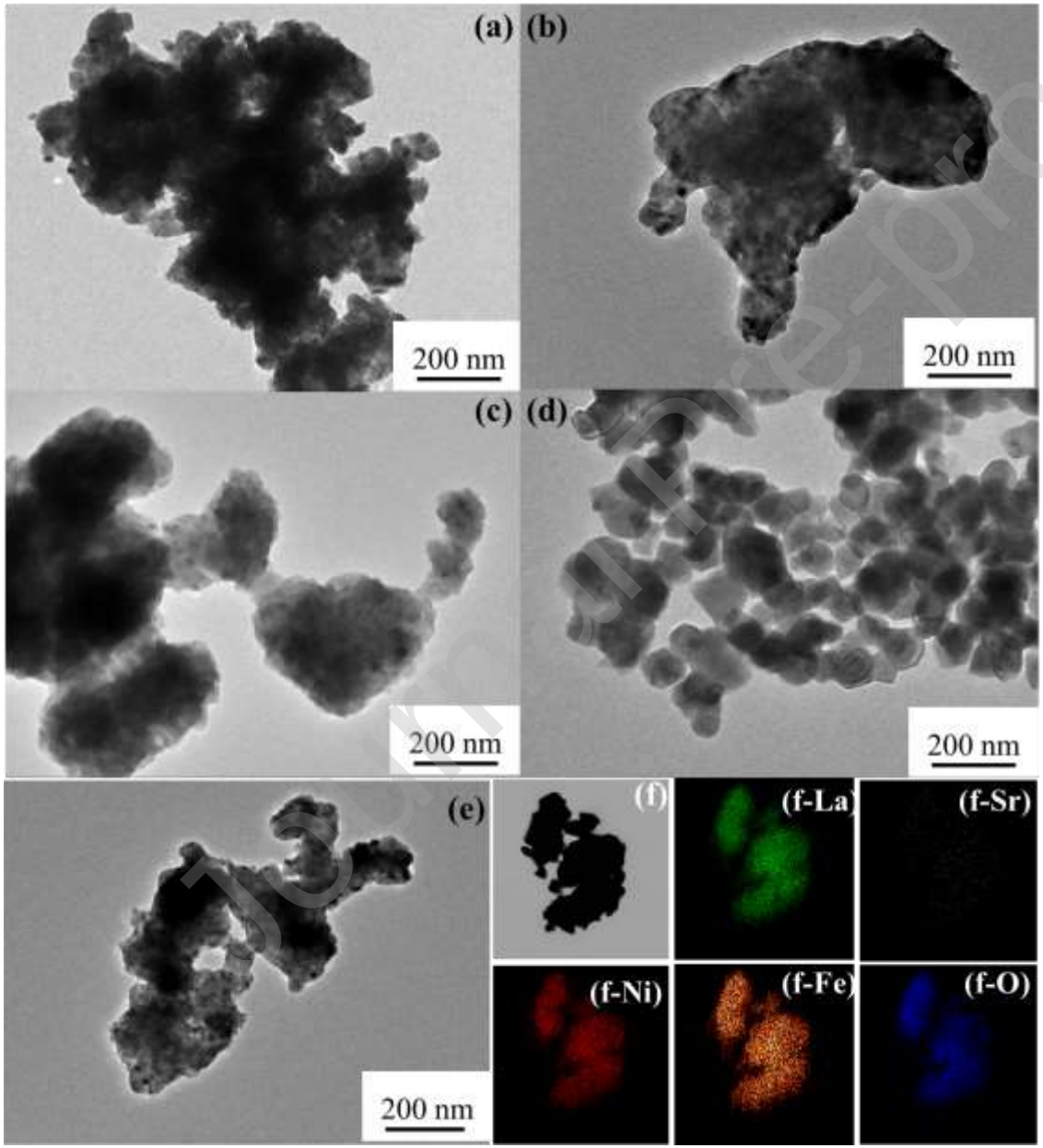

Fig. 3.

Fig. 4. (a) O_2-TPD and (b) CO_2-TPD profiles of reduced Ni/La_2O_3, LNO, LSNO and LSNFO catalysts.

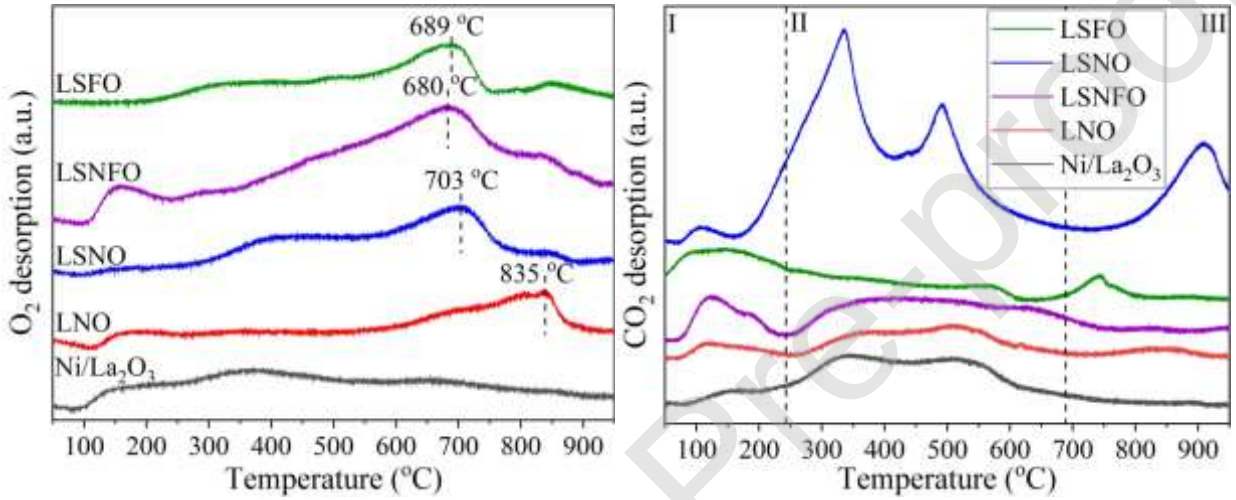

(a) (b)

Fig. 4.

Fig. 5. Typical (a) O1s and (b) Ni 2p XPS spectra of reduced Ni/La_2O_3, LNO, LSNO and LSNFO catalysts.

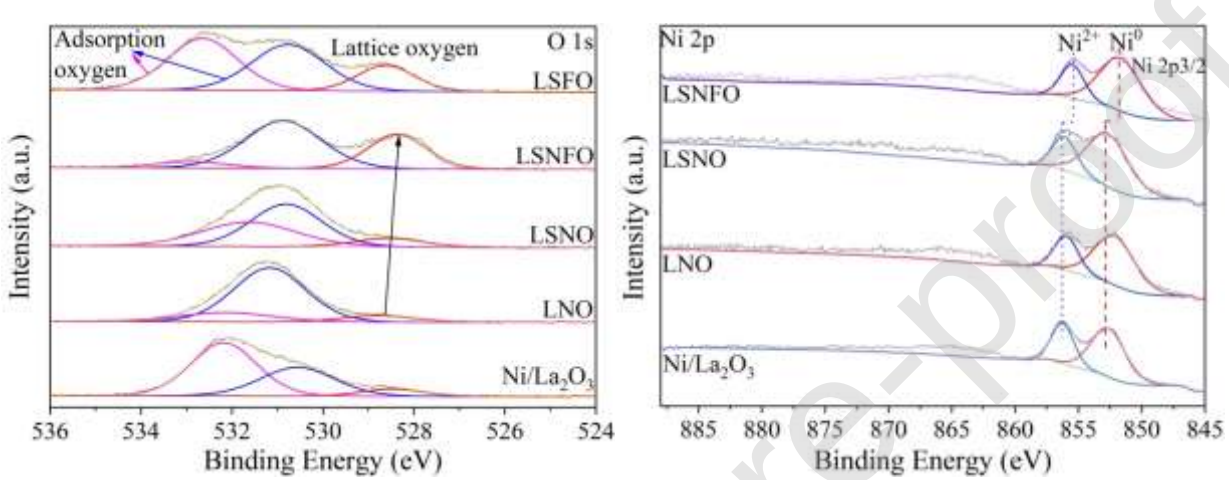

(a) (b)

Fig. 5.

Fig. 6. XANES (a) Ni K-edge and (b) Fe K-edge spectra of reduced LSNFO catalyst, standard Ni foil, NiO, Fe foil, FeO and Fe_2O_3, and (c) FT of Ni and Fe K-edge EXAFS spectra of reduced LSNFO, LNO and standard Ni and Fe foils.

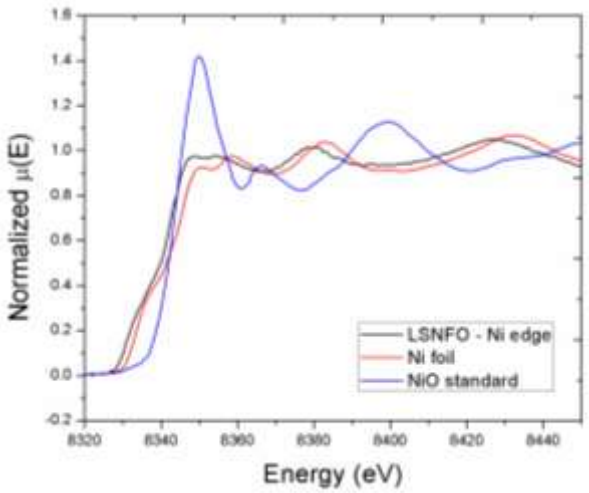

(a)

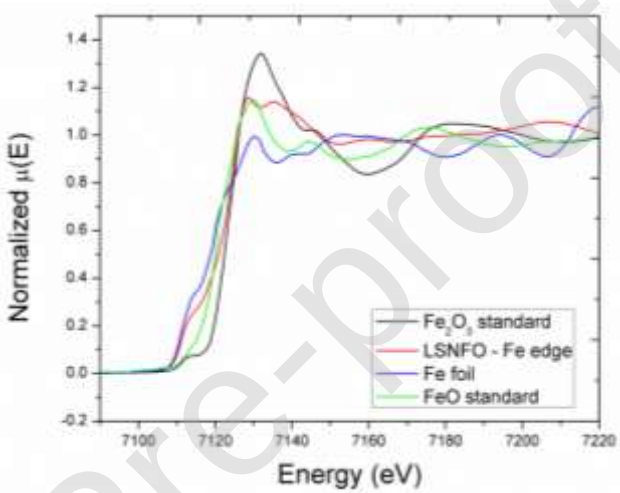

(b)

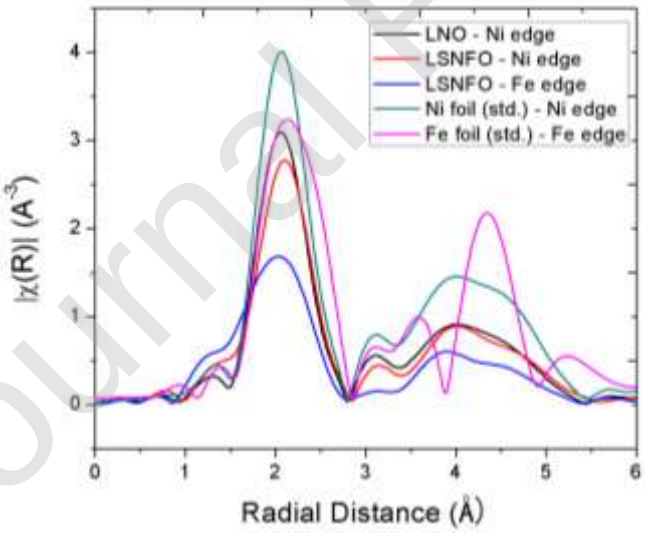

(c)

Fig. 6.

Fig. 7. (a) Conversion of CO_2, selectivity of (b) CO and (c) CH_4 and (d) carbon balance in plasma-catalysis system and (e) performance of LSNFO for RWGS in thermal-catalysis system (Condition: H_2/CO_2/He: 10/10/10 mL/min, Catalyst weight: 100 mg).

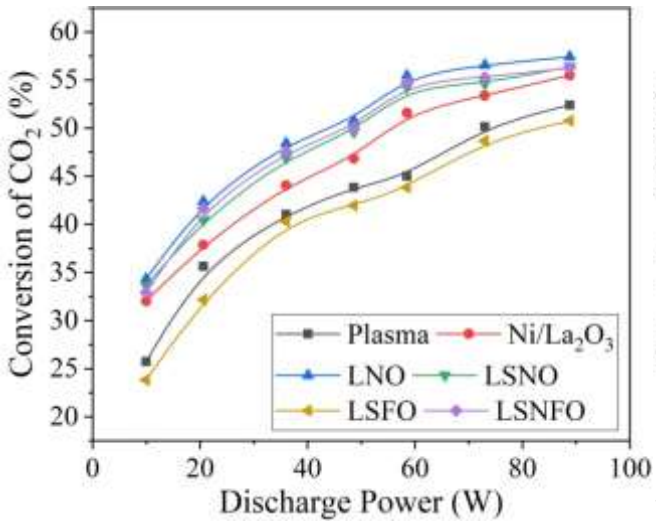

(a)

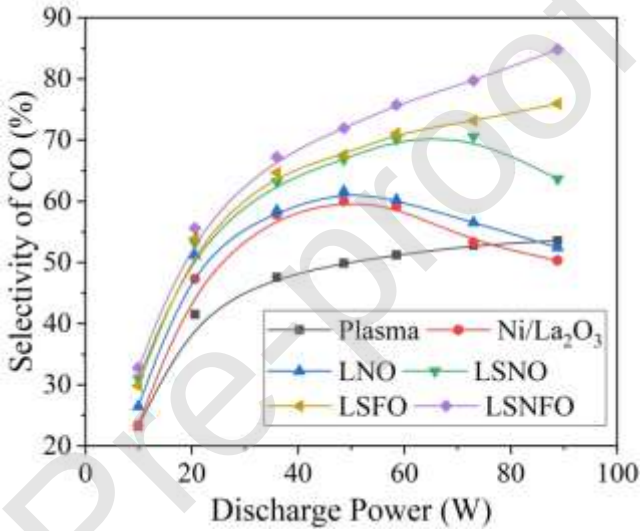

(b)

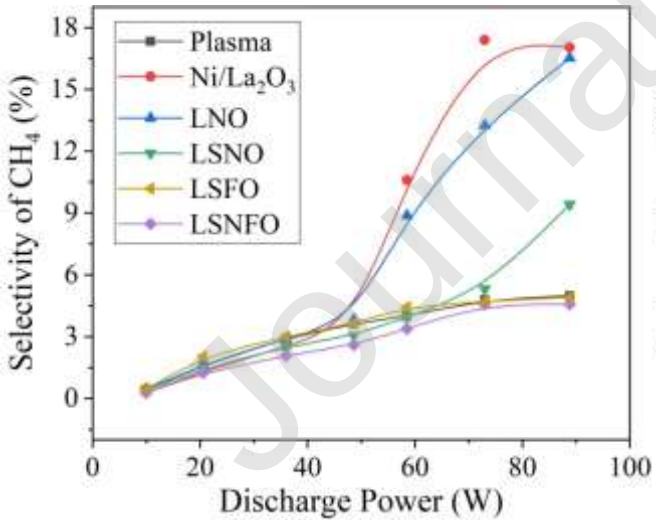

(c)

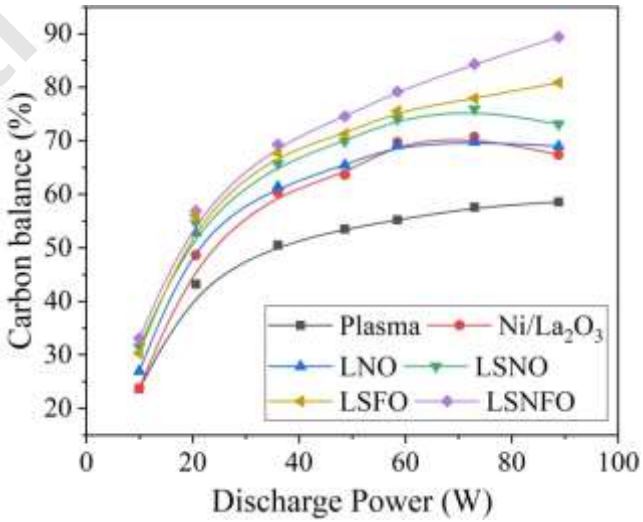

(d)

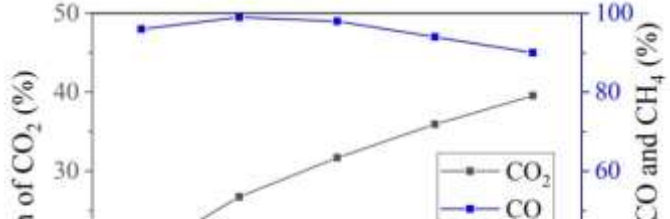

Fig. 8. Effect of H_2 to CO ratio on the (a) conversion of CO_2, selectivity of (b) CO and (c) CH_4 and yield of CO over LSNFO (Condition: H_2/CO_2/He: 4~16/16~4/10 mL/min, Catalyst: LSNFO, Catalyst weight: 100 mg)

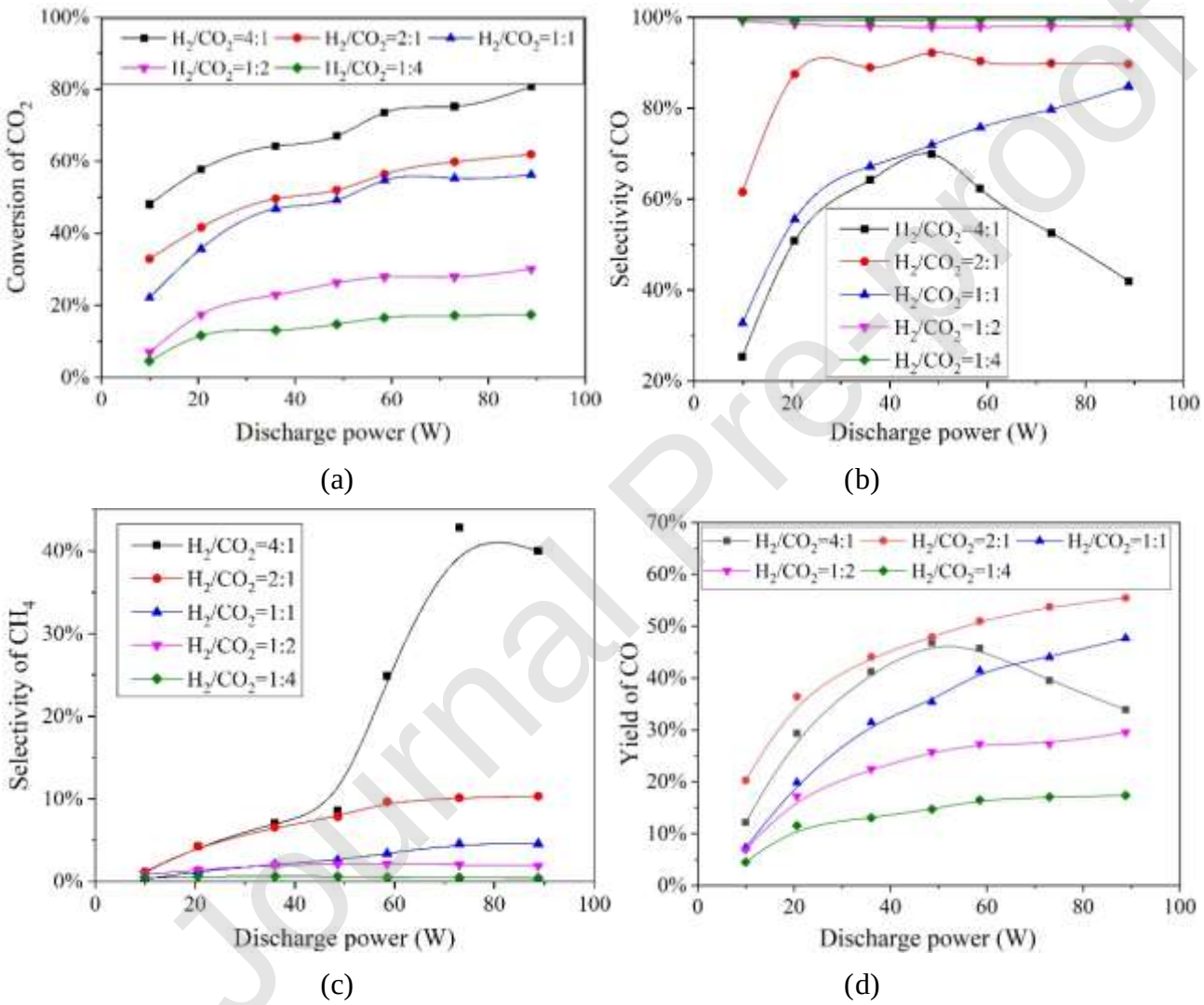
Conversion of CO_2
Discharge power (W)
H_2/CO_2=4:1
H_2/CO_2=2:1
H_2/CO_2=1:1
H_2/CO_2=1:2
H_2/CO_2=1:4
(a)
Selectivity of CO
Discharge power (W)
(b)
Selectivity of CH_4
Discharge power (W)
(c)
Yield of CO
Discharge power (W)
(d)

Fig. 8.

Table 1. Textural Properties of fresh and reduced catalysts.

	S_{BET}[a] (m^2/g)		V_p[a] (cm^3/g)		D_p[a] (nm)		Metal particle size[b] (nm)	H_2 consumption[c] (mmol/g)	Ni-based reduction degree (%)	Reduced Fe amount[d] (mmol/g)	Average metal particle size[e] (nm)	Ni dispersion[f] (%)	Estimated Ni particle size[g] (nm)
Catalysts	Fresh	Reduced	Fresh	Reduced	Fresh	Reduced							
Ni/La_2O_3	0.7	2.3	0.003	0.005	14.9	19.3	26.6	4.12	101.2	-	23.2	3.41	29.3
LNO	4.2	22.1	0.017	0.083	17.2	15.0	19.7	3.94	96.8	-	16.3	4.31	23.2
LSNO	15.8	16.0	0.060	0.058	15.0	14.7	16.9	4.06	97.6	-	13.1	4.98	20.0
LSFO	6.7	7.1	0.031	0.035	19.2	18.1	-	0.39	-	0.26	-	-	-
LSNFO	6.6	8.8	0.016	0.038	17.6	18.4	13.9	2.32	111.0	0.15	9.9	9.19	10.9

[a] Measured by N_2 adsorption-desorption isotherm.

[b] Calculated from XRD by Debye-Scherrer Equation.

[c] H_2 consumption below 700 °C in TPR profiles as shown in Fig. 3.

[d] H_2 consumption exceeded 100% is assigned to the reduction of Fe.

[e] Determined by the TEM results.

[f] Determined by the H_2-chemisoprtion analysis.

[g] Calculated based on H_2-chemisorption results.

Table 2. Composition of surface oxygen species.

Catalyst	Surface oxygen species						Surface Ni species			
	Lattice oxygen		Adsorbed oxygen		Adsorbed H_2O		Ni^0		Ni^{2+}	
	B.E. (eV)	% area	B.E. (eV)	% area	B.E. (eV)	% area	B.E. (eV)	% area	B.E. (eV)	% area
Ni/La_2O_3	528.48	7.30	530.56	34.92	532.18	57.78	852.63	64.97	856.21	35.03
LNO	528.77	8.78	531.07	75.02	532.13	16.20	852.12	70.98	855.92	29.02
LSNO	528.55	10.22	530.81	50.77	531.63	39.01	852.63	73.43	856.07	26.57
LSNFO	528.36	33.05	530.87	59.64	532.89	7.31	851.66	74.19	855.46	25.81
LSFO	528.62	17.31	530.76	39.89	532.64	42.80	-	-	-	-

Table 3. Performance of hybrid DBD plasma-$La_{0.9}Sr_{0.1}Ni_{0.5}Fe_{0.5}O_{3+\delta}$ system compared with state-of-the-art catalysts for RWGS reaction.

System	Catalyst	T (°C)	P (MPa)	H_2/CO_2	CO_2 conversion (%)	CO selectivity (%)	CO yield (%)	TOF[a] (s^{-1})	Stability	Ref.
Thermal-catalysis	Cu/β-Mo_2C	600	0.1	2:1	40	99.2	39.7	3.7	The catalyst maintained 85% of its initial activity after 40h.	[1]
Thermal-catalysis	Ir(0.1wt%)/TiO_2	350	0.1	1:1	2.1	100	2.1	0.043	N.A.	[11]
Thermal-catalysis	K_{80}-Pt/L	500	0.1	1:1	27.4	>95%	26	2.25	N.A.	[13]
Integrated CO_2 capture and utilization	$Ca_1Ni_{0.1}Ce_{0.033}$	650	0.1	N.A.	51.8	~100	51.8	0.78	The material exhibited superior cyclic stability after 20 cycles.	[54]
Thermal-catalysis	Au/TiO_2	350	0.1	4:1	27			0.24	N.A.	[21]
Thermal-catalysis	Co/Mo_2C	300	0.1	2:1	9.5	98.1	9.3	0.27	Activity and selectivity did not decrease for 36h.	[55]
Thermal-catalysis	CuO_x/CeO_2	400	0.1	1:1	16	100	16	N.A.	The conversion decreased to 9% after 20h on stream.	[58]
Thermal-catalysis	Ni-Fe_2O_3/CeO_2-Al_2O_3	600	0.1	4:1	~64	~55	35	N.A.	NiFe/CeAl remains approximately 70% of its initial CO_2 conversion over 48 h continuous test.	[4]
Thermal-catalysis	Fe-Cu-Cs/Al_2O_3	500	0.1	4:1	~55	>99	57	N.A.	CO_2 conversion remains constant at ~55% for 50 h with CO selectivity of >99%.	[57]
Thermal-catalysis	CsFe/Al_2O_3	600	0.1	1:1	~45	~75	34	N.A.	N.A.	[56]
Plasma-catalysis	Cu/γ-Al_2O_3	30	0.1	3:1	21.1	~40	8.4	0.004	The performance is stable for 6h	[51]

									continuous running.	
Thermal-catalysis	LSNFO	600	0.1	1:1	40	90	36	0.14	N.A.	This work
Plasma-only	No catalyst	120	0.1	1:1	52	54	28.1	N.A.	N.A.	This work
Plasma-catalysis	LSNFO	120	0.1	1:1	56	84	47	0.18	N.A.	This work
Plasma-catalysis	LSNFO	120	0.1	2:1	60	90	54	0.21	No deactivation was observed after 100h.	This work

[a] *TOF, turnover frequency, which is defined as the ratio of moles of CO produced per mole of active metal per second to the dispersion of active metals.*